

# 1 Influence of Photochemical Loss of VOCs on Understanding Ozone 2 Formation Mechanism

3 Wei Ma<sup>1</sup>, Zemin Feng<sup>1,7</sup>, Junlei Zhan<sup>1</sup>, Yongchun Liu<sup>1\*</sup>, Pengfei Liu<sup>2,4,5</sup>, Chengtang Liu<sup>2,4,5</sup>, Qingxin  
4 Ma<sup>2,4,5</sup>, Kang Yang<sup>3</sup>, Yafei Wang<sup>3</sup>, Hong He<sup>2,4,5</sup>, Markku Kulmala<sup>1,6</sup>, Yujing Mu<sup>2,4,5</sup>, Junfeng Liu<sup>2,4,5\*</sup>

5 1. Aerosol and Haze Laboratory, Advanced Innovation Center for Soft Matter Science and Engineering,  
6 Beijing University of Chemical Technology, Beijing, 100029, China

7 2. Research Center for Eco-Environmental Sciences, Chinese Academy of Sciences, Beijing, 100085, China

8 3. Beijing Institute of Petrochemical Technology, Beijing 102617, China

9 4. Center for Excellence in Regional Atmospheric Environment, Institute of Urban Environment, Chinese  
10 Academy of Sciences, Xiamen 361021, China

11 5. University of Chinese Academy of Sciences, Beijing 100049, China

12 6. Institute for Atmospheric and Earth System Research, Faculty of Science, University of Helsinki, Helsinki,  
13 00014, Finland

14 7. College of Chemical Engineering, North China University of Science and Technology, Tangshan 063021,  
15 China

16 \*Corresponding to: Yongchun Liu (liuyc@buct.edu.cn) and Junfeng Liu (junfengliu@rcees.ac.cn)

17

18 **Abstract**

19 Volatile organic compounds (VOCs) tend to be consumed by atmospheric oxidants,  
20 resulting in substantial photochemical loss during transport. An observation-based model was  
21 used to evaluate the influence of photochemical loss of VOCs on the sensitivity regime and  
22 mechanisms of ozone formation. Our results showed that a VOC-limited regime based on  
23 observed VOC concentrations shifted to a transition regime with a photochemical initial  
24 concentration of VOCs (PIC-VOCs) in the morning. The net ozone formation rate was  
25 underestimated by  $3 \text{ ppb h}^{-1}$  ( $\sim 36 \text{ ppb day}^{-1}$ ) based on the PIC-VOCs. The relative contribution  
26 of the  $\text{RO}_2$  path to ozone production based on the PIC-VOCs accordingly increased by 13.4%;  
27 in particular, the contribution of alkene-derived  $\text{RO}_2$  increased by approximately 10.2%. In  
28 addition, the OH- $\text{HO}_2$  radical cycle was obviously accelerated by highly reactive alkenes after  
29 accounting for photochemical loss of VOCs. The contribution of local photochemistry might  
30 be underestimated for both local and regional ozone pollution if consumed VOCs are not  
31 accounted for, and policymaking on ozone pollution prevention should focus on VOCs with a  
32 high reactivity.

33

## 34 **1. Introduction**

35 Ground surface ozone ( $O_3$ ) is an important atmospheric pollutant that is harmful to human  
36 health and is connected with respiratory, cardiovascular diseases, and premature mortality  
37 (Cohen et al., 2017). It is also harmful to vegetation growth. For example, it led to annual  
38 reductions in the yields of rice and wheat by 8% and 6%, respectively, and reduced forest  
39 biomass growth by 11-13% in China (Feng et al., 2019). Surface  $O_3$  concentrations have  
40 increased by 11.9% over eastern China despite the air pollution control measures implemented  
41 in China from 2012 to 2017 (Dang and Liao, 2019). An economic loss of 0.09% of the Chinese  
42 gross domestic product (78 billion CNY) is predicted for 2030 if policies against  $O_3$  pollution  
43 are not properly implemented (Xie et al., 2019). Therefore, urgent action to minimize  $O_3$   
44 pollution in China is needed.

45 Tropospheric  $O_3$  is mainly produced from photochemical reactions between volatile  
46 organic compounds (VOCs) and nitrogen oxides ( $NO_x$ :  $NO+NO_2$ ) (Seinfeld and Pandis, 2006;  
47 Liu et al., 2021).  $O_3$  is generated from a collision of  $O_2$  and  $O(3P)$  that is produced from  
48 photolysis of  $NO_2$  in the atmosphere. Peroxyl radicals ( $HO_2$  and  $RO_2$ ), which are produced  
49 from the oxidation of VOCs by OH radical, can efficiently convert NO (from the photolysis of  
50  $NO_2$ ) to  $NO_2$ , leading to a net  $O_3$  production by compensating for the titration of  $O_3$  by NO  
51 (Monks, 2005; Zhang et al., 2021a). Over the past two decades, a number of field observations  
52 focused on  $O_3$  pollution levels and its precursors have been carried out in the Beijing-Tianjin-  
53 Hebei (BTH), Yangtze River Delta (YRD), and Pearl River Delta (PRD) regions (Wang et al.,  
54 2017; Li et al., 2019; Xue et al., 2014; Zhang et al., 2019). Due to the nonlinear relationship

55 between O<sub>3</sub> and its precursors and the variations in meteorological conditions, numerous  
56 studies have been performed to understand the sensitivity regime of O<sub>3</sub> formation (Ling and  
57 Guo, 2014; Zhang et al., 2020), the photochemical process of O<sub>3</sub> formation based on box  
58 models or observation-based models (OBM) (He et al., 2019; Tan et al., 2019), and the sources  
59 of O<sub>3</sub> using regional chemical transport models (Li et al., 2016b; Li et al., 2016c). Recently,  
60 the instantaneous production rate of the O<sub>3</sub> formation process has attracted more attention; for  
61 example, studies examining radical recycling (OH-RO<sub>2</sub>-RO-HO<sub>2</sub>-OH) related to the production  
62 of O<sub>3</sub> have been performed (Lu et al., 2017; Tan et al., 2017; Whalley et al., 2018). HCHO  
63 photolysis and alkene ozonolysis contributed approximately 85% to the primary production of  
64 HO<sub>2</sub> and HO radicals in Beijing, Shanghai and Guangzhou (Tan et al., 2019; Yang et al., 2017).  
65 The importance of HONO and HCHO photolysis for primary radical production has also been  
66 proposed in suburban and rural areas (Tan et al., 2017; Lu et al., 2012; Lu et al., 2013).

67 All of the OBM studies investigating the relationship between O<sub>3</sub> and VOCs were based  
68 on measured datasets. However, VOCs are highly reactive to atmospheric oxidants, such as  
69 OH, NO<sub>3</sub>, and O<sub>3</sub>, among which OH is dominant. The lifetimes of some highly reactive VOCs,  
70 such as isoprene, are as short as only a few tens of minutes under typical daytime atmospheric  
71 conditions. The mixing ratios of VOCs observed at a sampling site are actually the residues of  
72 VOCs from emissions due to the photochemical loss during transport from the source site to  
73 the receptor site. If photochemically consumed VOCs are not considered, the O<sub>3</sub> formation  
74 sensitivity and net O<sub>3</sub> production may be misunderstood, and subsequent policymaking on O<sub>3</sub>  
75 pollution prevention at regional or urban scales may be misguided. Thus, the photochemical

76 age-based approach has been applied to evaluate the effect of photochemical processes on VOC  
77 measurements (Shao et al., 2011). This method was used to qualitatively or semi-quantitatively  
78 estimate the O<sub>3</sub> formation process of the source-receptor (Gao et al., 2018) by calculating the  
79 O<sub>3</sub> formation potential (OFP) (Han et al., 2017), identifying the critical species for O<sub>3</sub> formation  
80 (Gao et al., 2021), or evaluating the VOC emissions ratio (Yuan et al., 2013). In evaluating the  
81 importance of initial VOCs to ozone production, Xie et al. (2008) found that the OFP at a  
82 Peking University site increased by 70% after accounting for the photochemical loss of VOCs.  
83 Li et al. (2015) also showed that the OFPs of total NMHCs (excluding isoprene) increased by  
84 16.1% (from 59.6 to 69.2 ppb O<sub>3</sub>), 12.1% (from 33.5 to 37.5 ppb O<sub>3</sub>), and 3.4% (from 68.9 to  
85 71.2 ppb O<sub>3</sub>) after correcting for photochemical loss in Gucheng, Quzhou, and Beijing,  
86 respectively. Gao et al. (2018) reported that the OFP could be underestimated by 23.4% (62.4  
87 ppb O<sub>3</sub>) in Beijing if the photochemical loss of VOCs is not considered. Zhan et al. (2021)  
88 found that based on measured VOCs, the OFP increased from 57.8 ppb to 103.9 ppb using the  
89 initial VOCs. All the previous work was based on the maximum incremental reactivities (MIR)  
90 method. The application of such calculations using the MIR method is restricted to areas or  
91 episodes in which O<sub>3</sub> formation is VOC-sensitive (Carter, 1994). In the troposphere, the  
92 sensitivity of ozone formation to NO<sub>x</sub> and VOCs varies greatly, as evidenced by the wide range  
93 of OFP underestimations from ~3% to 70% in previous work. **In addition, the MIR values of**  
94 **VOC species for a specific region are calculated with the base scenario, in which NO**  
95 **concentration and other parameters are the values that correspond to the maximal incremental**  
96 **reactivity (IR). The fixed MIR values of different VOCs can neither reflect the non-linear**

97 relationship between ozone and VOCs, involving in the complicated radical recycling (OH-  
98 RO<sub>2</sub>-RO-HO<sub>2</sub>-OH) related to the production of ozone, nor be used for analyzing the radical  
99 budget of the initial VOCs concentration. Thus, a quantitative analysis is necessary to explicitly  
100 understand the influence of photochemical loss of VOCs on ozone formation and its  
101 mechanism based on OBM studies, in which the dynamic atmospheric and meteorological  
102 conditions is accounted for.

103 In this study, an OBM was used to evaluate the local O<sub>3</sub> formation process in summer in  
104 Beijing based on concentrations of observed and photochemical initial concentrations of VOCs  
105 (PIC-VOCs). The O<sub>3</sub>-NO<sub>x</sub>-VOC sensitivity, instantaneous O<sub>3</sub> formation rate and in situ O<sub>3</sub>  
106 formation process were discussed. The aim of this study was to understand the possible  
107 influence of photochemical loss of VOCs on the formation sensitivity regime of O<sub>3</sub> and how  
108 the photochemical loss of VOCs affects O<sub>3</sub> formation. This study can provide new insight for  
109 better understanding atmospheric O<sub>3</sub> pollution.

## 110 **2. Methodology**

### 111 **2.1 Experimental section**

112 Field observations were carried out on the Qingyuan campus of the Beijing Institute of  
113 Petrochemical Technology (BIPT, 39.73°N and 116.33°E) (Figure S1). Details on the  
114 observation site have been described in our previous work (Zhan et al., 2021). In short, the site  
115 is a typical suburban site in the Daxing District between 5<sup>th</sup> Ring Road and 6<sup>th</sup> Ring Road. The  
116 field campaign was carried out during August 1-28, 2019, when photochemistry was the most  
117 active and rainfall was rare in Beijing.

118 The concentrations of nonmethane hydrocarbons (NMHCs) were detected by both a gas  
119 chromatography-flame ionization detector (GC/FID) and a single photon ionization (SPI) TOF-  
120 MS (SPI-MS 3000, Guangzhou Hexin Instrument Co., Ltd., China). A detailed description of  
121 the instrumentation can be found in previous publications (Zhan et al., 2021; Chen et al., 2020).  
122 The SPI-MS was also used to detect halohydrocarbons. More details on this instrument and its  
123 parameter settings have been described in previous studies (Zhang et al., 2019; Liu et al.,  
124 2020a). In short, a 0.002 int thick polydimethylsiloxane (PDMS) membrane (Technical  
125 Products Inc., USA) was used to collect VOCs and diffuse them from the sample site to the  
126 detector under high vacuum conditions. Vacuum ultraviolet (VUV) light generated by a  
127 commercial D2 lamp (Hamamatsu, Japan) was utilized for ionization at 10.8 eV. For ion  
128 detection, two microchannel plates (MCPs, Hamamatsu, Japan) assembled with a chevron-type  
129 configuration were employed. This TOF-MS has an LOD varying from 50 ppt to 1 ppb with a  
130 1-minute time resolution for most trace gases without any preconcentration procedure. To  
131 verify the data compatibility of the SPIMS and GC/FID, we compared the concentrations of  
132 toluene measured using these two different instruments (Figure S2). The correlation coefficient  
133 was 0.9 (with a slope of 0.7), indicating that the concentrations of NMHCs were comparable  
134 using these two measurement techniques.

135 Oxygenated VOCs (OVOCs) were collected using 2,4-dinitrophenylhydrazine (DNPH)-  
136 coated silica gel cartridges (Sep-Pak, Waters) by an automatic sampling device with a sampling  
137 flow rate of 1.2 L min<sup>-1</sup> and a duration of 2 h for each sample. Then, the OVOCs were analysed  
138 using high-performance liquid chromatography (HPLC, Inertsil ODS-P 5 µm 4.6 × 250 mm

139 column, GL Sciences) with an acetonitrile-water binary mobile phase (Ma et al., 2019). To  
140 avoid possible contamination or desorption after sampling, cartridges were capped, placed into  
141 tightly closed plastic bags and kept in a refrigerator before analysis. The sampled cartridges  
142 were eluted with 5 mL acetonitrile and analysed by HPLC as soon as possible after they were  
143 shipped back to the laboratory. This system was calibrated with 8-gradient standard solutions  
144 (TO11/IP-6A Aldehyde/Ketone-DNPH Mix, SUPELCO). The correlation coefficients were all  
145 greater than 0.999. The LOD for most OVOCs was approximately 10 ppt.

146 Trace gases, including NO<sub>x</sub>, SO<sub>2</sub>, CO, and O<sub>3</sub>, were measured using corresponding  
147 analysers (Thermo Scientific, 42i, 43i, 48i, and 49i, respectively). The HONO concentration  
148 was measured using a homemade long path absorption photometer (LOPAP) (Liu et al., 2020c).  
149 The meteorological parameters, including temperature (T), pressure (P), relative humidity  
150 (RH), wind speed, and wind direction, were measured by a weather station (AWS310, Vaisala).  
151 The photolysis rate ( $J_{NO_2}$ ) was measured via continuous measurement of the actinic flux in the  
152 wavelength range of 285-375 nm using a  $J_{NO_2}$  filter radiometer ( $J_{NO_2}$  radiometer, Metcon).

## 153 **2.2 Calculation of photochemical loss of VOCs**

154 The photochemical loss of VOCs was calculated using the ratio method (Wiedinmyer et  
155 al., 2001; Yuan et al., 2013). The initial mixing ratio of a specific VOC was calculated using  
156 the following equations (Mckeen et al., 1996):

$$157 \quad [VOC_i]_t = [VOC_i]_{t0} \times \exp(-k_i \times [OH] \times \Delta t) \quad (1)$$

$$158 \quad \Delta t = \frac{1}{[OH] \times (k_X - k_E)} \times \left\{ \ln \left( \frac{X_0}{E_0} \right) - \ln \left( \frac{X_t}{E_t} \right) \right\} \quad (2)$$

159 where  $[VOC_i]_t$  and  $[VOC_i]_{t0}$  are the observed and initial concentrations of  $VOC_i$ , respectively;



160  $k_i$  is the second-order reaction rate between compound  $i$  and OH radical; and  $[OH]$  and  $\Delta t$  are  
161 the concentration of OH radical and the photochemical ageing time, respectively.  $k_X$  and  $k_E$  are  
162 rate constants for the reaction between OH radicals and ethylbenzene ( $7.00 \times 10^{-12} \text{ cm}^3$   
163  $\text{molecule}^{-1} \text{ s}^{-1}$ ) and xylene ( $1.87 \times 10^{-11} \text{ cm}^3 \text{ molecule}^{-1} \text{ s}^{-1}$ ) (Atkinson and Arey, 2003),  
164 respectively. ( $X_0/E_0$ ) is the initial mixing ratio between xylene and ethylbenzene, and ( $X_i/E_i$ ) is  
165 the mixing ratio between xylene and ethylbenzene at the observation time. In this study, we  
166 chose the mean concentrations of xylene and ethylbenzene at 05:00-06:00 as their initial  
167 concentrations before sunrise according to the ambient  $J_{NO_2}$  (Figure S3) to calculate the  
168 photochemical loss of OH exposure. In previous work (Shao et al., 2011; Zhan et al., 2021),  
169 the selection of ethylbenzene and xylene as tracers was justified for calculating ambient OH  
170 exposure under the following conditions: 1) the concentrations of xylene and ethylbenzene  
171 were well correlated (Figure S4), which indicated that they were simultaneously emitted; 2)  
172 they had different degradation rates in the atmosphere; and 3) the calculated PICs were in good  
173 agreement with those calculated using other tracers, such as i-butene/propene (Figure S5)  
174 (Zhan et al., 2021). To test the relative constant emission ratio from different sources, we chose  
175 benzene vs. acetylene and n-hexane vs. toluene as references, and the result is shown in Figure  
176 S6. These ambient ratios could directly reflect their relative emission rates from sources  
177 (Goldan et al., 2000; Jobson et al., 2004). The linear correlation coefficients ( $R^2$ ) were generally  
178 higher than 0.7, which were equal to that reported by Shao et al. (2011). To further test the  
179 assumption that the emissions of xylene and ethylbenzene were constant throughout the day,  
180 their potential sources were calculated using a source-receptor model (the potential source

181 contribution function, PSCF). As shown in Figure S7, xylene and ethylbenzene showed similar  
182 distributions. In addition, the ratio of ethylbenzene/xylene at 5:00 and 6:00 was similar to that  
183 during the daytime. These results indicated that the emissions of xylene and ethylbenzene were  
184 constant throughout the day. The ratio of xylene to ethylbenzene and the OH exposure  
185 concentration are shown in Figure S8. The results showed that the ratio of xylene to  
186 ethylbenzene increased gradually (07:00~12:00), which is consistent with the trend of xylene  
187 and ethylbenzene. The OH exposure was from  $0.82$  to  $8.1 \times 10^6$  molecule  $\text{cm}^{-3}$  h, with a mean  
188 daytime value of  $4.3 \pm 1.9 \times 10^6$  molecules  $\text{cm}^{-3}$  h. Accordingly, the mean photochemical ages  
189 were  $1.7 \pm 0.9$  h using the mean daytime (8:00-17:00 LT) OH concentrations ( $4.3 \pm 3.1 \times 10^6$   
190 molecules  $\text{cm}^{-3}$ ) calculated based on JO1D using the method reported in our previous work  
191 (Liu et al., 2020b; Liu et al., 2020c). This meant that VOCs would undergo obvious degradation  
192 even during a short range of transport in the atmosphere.

193 It should be noted that the  $k_{OH}$  of isoprene is  $9.98 \times 10^{-11}$   $\text{cm}^3$  molecule $^{-1}$  s $^{-1}$  at 298.15 K  
194 (Atkinson and Arey, 2003), almost two orders of magnitude greater than other VOCs. The ratio  
195 method assumes constant emissions for VOCs. However, the emission of isoprene greatly  
196 depends on temperature and solar irradiation intensity (Zhang et al., 2021b). In addition to  
197 accounting for photochemical loss, additional correction of daytime isoprene concentrations  
198 was performed using the average diurnal flux of isoprene emissions (Figure S9 (Zhang et al.,  
199 2021b). The emission of isoprene showed a clear unimodal curve, and the volume  
200 concentration of isoprene was calculated based on the daily emission curve using Eq. (S1).

## 201 2.3 Observation-based model simulation

202 A box model based on the Master Chemical Mechanism (MCM3.3.1) and the Regional  
203 Atmospheric Chemical Mechanism (RACM2) was used in this study. The MCM3.3.1 was used  
204 to understand the instantaneous ozone formation process, and the RACM2 was used to depict  
205 the ozone isopleth due to its high computational efficiency (Sect. 2.4). Table S1 shows the  
206 model inputs. The model calculations were constrained with the measured meteorological  
207 parameters (RH, T, P, and  $J_{NO_2}$ ) and the concentrations of trace gases, including inorganic  
208 species (NO, NO<sub>2</sub>, CO, SO<sub>2</sub>, and HONO) and 61 organic species (NMHCs (46), OVOCs (8),  
209 and halohydrocarbons (7)). The model was validated using the observed and simulated O<sub>3</sub>  
210 concentrations, which showed good consistency, as shown in Figure S10. The slope and  
211 correlation coefficients were 0.9 and 0.8, respectively (Figure S11, respectively, indicating the  
212 validity of the model simulation. It is worth mentioning that the results of model simulation  
213 can sometimes be overestimated or underestimated to some extent, which has also been  
214 reported by previous studies (Zong et al., 2018; Zhang et al., 2020), but this did not affect our  
215 simulations of the ozone formation process and mechanisms because we constrained the ozone  
216 concentration during our simulations.

217 The ozone formation rate  $P(O_3)$  can be quantified by the oxidation rate of NO to NO<sub>2</sub> by  
218 peroxy radicals (Tan et al., 2019), as expressed in Eq. (3). In this study, the modelled peroxy  
219 radical concentrations were used to calculate the ozone production rate.

$$220 \quad P(O_3) = k_{HO_2+NO}[HO_2][NO] + k_{RO_2+NO}[RO_2][NO] \quad (3)$$

221 where  $P(O_3)$  is the ozone formation rate;  $[HO_2]$  and  $[RO_2]$  are the number concentrations of

222  $HO_2$  and  $RO_2$  radicals;  $k_{HO_2+NO}$  is the second reaction rate between  $HO_2$  and  $NO$ ; and  $k_{RO_2+NO}$   
 223 is the second reaction rate for the reaction of  $RO_2$  and  $NO$ , which only produces  $RO$  and  $NO_2$ .  
 224 Once ozone forms, it will be consumed by  $OH$ ,  $HO_2$ , and alkenes. Additionally, some  $NO_2$  can  
 225 react with  $OH$ , resulting in the formation of nitrate before photolysis. The chemical loss of both  
 226  $O_3$  and  $NO_2$  is considered in the calculation of the net ozone production rate (Tan et al., 2019),

$$227 \quad L(O_3) = (k_{O_3+OH}[OH] + k_{O_3+HO_2}[HO_2] + k_{O_3+alkenes}[alkenes])[O_3] +$$

$$228 \quad k_{NO_2+OH}[NO_2][OH] \quad (4)$$

229 where  $L(O_3)$  is the ozone chemical loss rate;  $[OH]$  is the number concentration of  $OH$  radical;  
 230  $k_{O_3+OH}$ ,  $k_{O_3+HO_2}$ , and  $k_{O_3+alkenes}$  are the second-order reaction rate constants between  $O_3$  and  $OH$ ,  
 231  $HO_2$  and alkenes, respectively; and  $k_{NO_2+OH}$  is the second-order reaction rate constant between  
 232  $NO_2$  and  $OH$ . Finally,  $F(O_3)$  is the net ozone formation rate calculated by the difference between  
 233  $P(O_3)$  and  $L(O_3)$ , as expressed in Eq. (5),

$$234 \quad F(O_3) = P(O_3) - L(O_3) \quad (5)$$

## 235 **2.4 Empirical Kinetic Modelling Approach**

236 The empirical kinetic modelling approach (EKMA) used in this work is a set of imaginary  
 237 tests to reveal the dependence of photochemical oxidation products on the change in precursors.  
 238 We set up  $30 \times 30$  matrices by reducing or increasing the measured VOCs and  $NO_x$   
 239 concentrations in the model input. The resulting radical concentrations and ozone production  
 240 rates were calculated correspondingly.

241 At this stage, the observed VOCs were grouped into different lumped species according  
 242 to their RACM2 classification; more details can be found in a previous publication (Tan et al.,

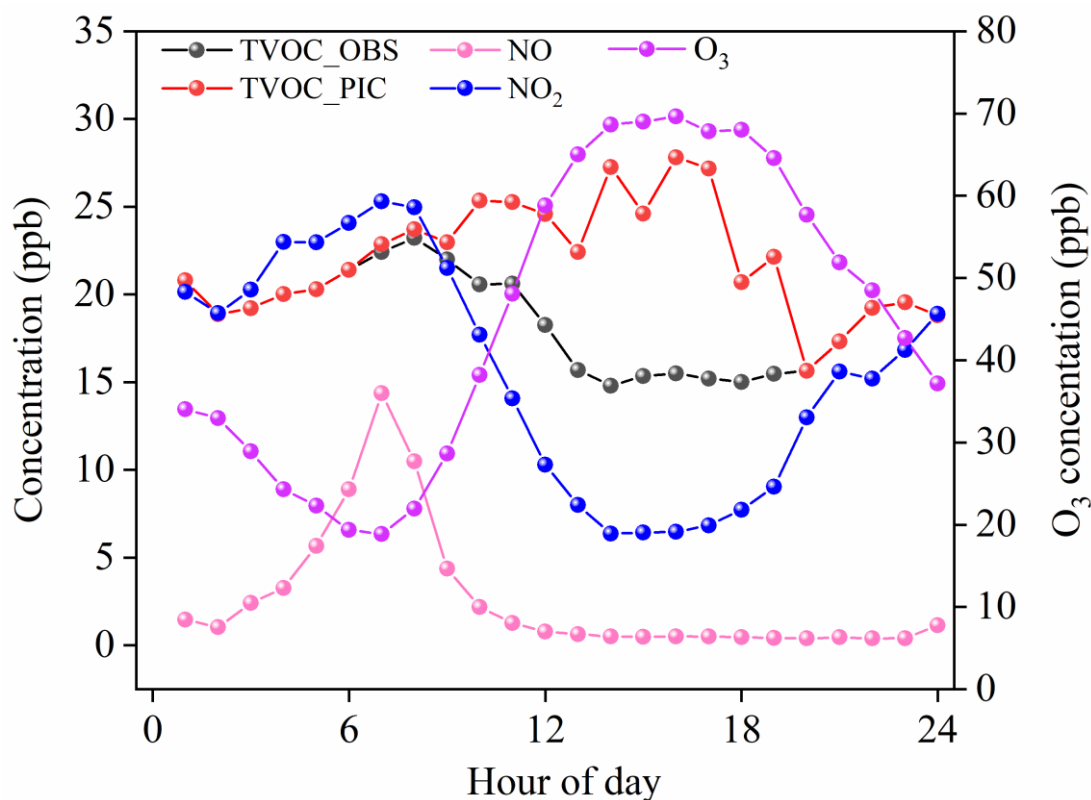
243 2017). The chemical model simulated photochemical reactions with input species for a time  
244 interval of 60 minutes, which was enough for NO<sub>x</sub>, OH, HO<sub>2</sub>, and RO<sub>2</sub> to reach a steady state  
245 because the typical relaxation time of the chemical system is 5-10 minutes in summer (Tan et  
246 al., 2018). However, all the species and parameters were input at a 5 min interval by data  
247 interpolation to reduce simulation inconsistencies and large distortions of meteorological  
248 parameters at longer time intervals (Tan et al., 2018). The ozone production rate was calculated  
249 as described in Sect. 2.3. It is worth mentioning that the average survey data were selected as  
250 the baseline scenario in simulating the EKMA curve in this study.

### 251 **3. Results and discussion**

#### 252 **3.1 Overview of diurnal variation in O<sub>3</sub>, NO<sub>x</sub>, and TVOC**

253 Figure 1 shows the average diurnal variation of concentrations in O<sub>3</sub>, NO<sub>x</sub>, and TVOC  
254 (including alkanes, alkenes, OVOCs, and halohydrocarbons) driven by emissions,  
255 photochemical reactions and the evolution of the mixing layer height (MLH). The ozone  
256 concentration during the observation period was  $44.8 \pm 27.2$  ppb with a maximum of 119.1 ppb,  
257 as reported in our previous study (Zhan et al., 2021), which was generally comparable with the  
258 O<sub>3</sub> concentrations during 2014-2018 (Ma et al., 2020). The O<sub>3</sub> followed a unimodal curve with  
259 a minimum value ( $18.8 \pm 15.4$  ppb) at 07:00 and then it increased to a maximum value (69.6  
260 ppb) at 15:00 as photochemical ozone formed. In contrast, NO<sub>x</sub> reached its maximum  
261 concentration ( $39.7 \pm 14.2$  ppb) at 07:00 and then decreased. After 07:00, the mixing ratio of  
262 NO continuously dropped, while the concentration of NO<sub>2</sub> decreased at first and then started  
263 to increase at 14:00. The diurnal variations in the observed TVOCs were generally consistent

264 with those of NO<sub>2</sub>. The observed TVOCs concentrations ranged from 2.2 to 23.2 ppb, with a  
 265 mean value of 18.6±2.6 ppb. Compared to the concentrations (45.4±15.2 ppb) in the same  
 266 period in August 2015 (Li et al., 2016a), the concentration of VOCs in Beijing was effectively  
 267 reduced. However, the photochemical initial concentrations (PICs) of TVOCs, which varied  
 268 from 2.2 to 27.8 ppb with a mean value of 24.5±2.1 ppb, showed a different diurnal curve  
 269 compared with the observed concentrations. It slightly increased from 07:00 to 14:00, which  
 270 was similar to the diurnal variation of VOCs in previous work (Zhan et al., 2021). The average  
 271 PIC-VOCs was 6.9±0.5 ppb higher than the observed concentration of TVOCs, indicating an  
 272 underestimated contribution of the local photochemistry of VOCs to O<sub>3</sub> and organic aerosol  
 273 formation.



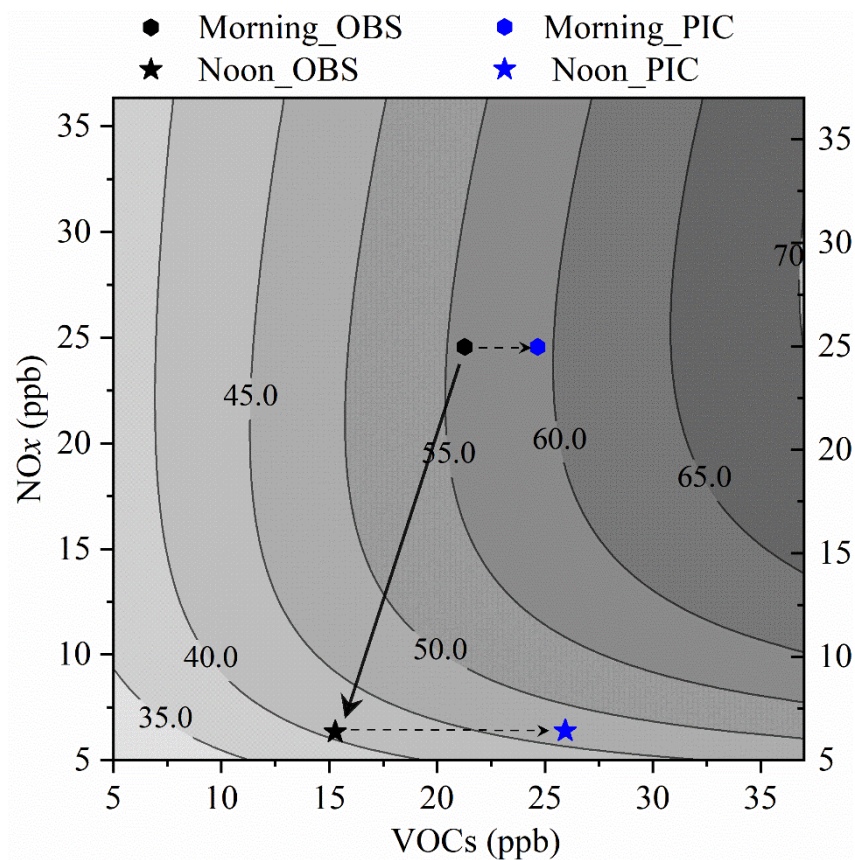
274  
 275 **Figure 1.** Overview of average diurnal variations in O<sub>3</sub>, NO<sub>x</sub>, and TVOC. The data represent  
 276 measured results, except for those of the TVOC\_PIC, which are calculated based on OH radical

277 exposure. The data range is August 1-28, 2019.

### 278 **3.2 Influence of photochemical loss of VOCs on the O<sub>3</sub> formation sensitivity regime**

279 The sensitivity of O<sub>3</sub> formation is analysed using the isopleth diagram generated from the  
280 EKMA model, which is widely used to qualitatively study O<sub>3</sub>-NO<sub>x</sub>-VOCs sensitivity. As  
281 described in Sect. 2.4, the concentrations of NO<sub>2</sub> and VOCs were artificially scaled to  $\pm 75\%$   
282 of the observed values to calculate the response of O<sub>3</sub> concentration to an imaginary change in  
283 the concentrations of NO<sub>2</sub> and VOC, with other constrained conditions remaining unchanged.  
284 Figure 2 shows the typical EKMA curves during our observations. The black stars and  
285 pentagons denote the observed concentrations of NO<sub>x</sub> and VOCs in the morning (09:00-10:00)  
286 and at noon (14:00-15:00), respectively, while the blue symbols are the corresponding values  
287 of PICs. Based on the measured data, O<sub>3</sub> formation was in a VOC-limited regime in the  
288 morning and a NO<sub>x</sub>-limited regime in the afternoon. The black arrow indicates a linearly  
289 decreasing trend of NO<sub>x</sub> and VOCs from 09:00 to 15:00 in the chemical coordinate system,  
290 and ozone production shifted from VOC-limited to NO<sub>x</sub>-limited conditions from morning to  
291 afternoon, which was consistent with the mean diurnal profiles (Figure 1). This was similar to  
292 the data reported in Wangdu (Tan et al., 2018). As expected, ozone production shifted from a  
293 VOC-limited regime (the observed VOCs) to a transition regime based on the PIC-VOCs in  
294 the morning. Ozone production clearly moved further to a NO<sub>x</sub>-limited regime in the afternoon  
295 after the photochemically consumed NO<sub>x</sub> and VOCs had been accounted for (Figure 2).  
296 Because the average photochemical ageing time was only  $1.7 \pm 0.9$  h, these results indicated  
297 that the O<sub>3</sub> formation mechanism might typically be misdiagnosed, which misleads mitigation

298 measures for O<sub>3</sub> prevention if the consumed VOCs under real atmospheric conditions are not  
299 considered.



300  
301 **Figure 2.** Isopleth diagram of the ozone concentration as a function of the concentration of  
302 NO<sub>x</sub> and VOCs derived from an empirical kinetic modelling approach. The pentagons and stars  
303 indicate the status in the morning (09:00-10:00) and at noon (14:00-15:00), respectively. The  
304 black and blue colours represent the observed and corrected statuses, respectively.

### 305 3.3 Contribution of VOC species to O<sub>3</sub> production

306 The time series of simulated OH, HO<sub>2</sub>, and RO<sub>2</sub> concentrations were used to calculate the  
307  $P(O_3)$  and  $L(O_3)$ . The diurnally averaged  $P(O_3)$  and  $L(O_3)$  are shown in Figure 3. Ozone  
308 formation can be divided into processes related to RO<sub>2</sub>+NO and HO<sub>2</sub>+NO (Sect. 2.3).  
309 According to their VOC precursors, peroxy radical groups were divided into alkane-derived



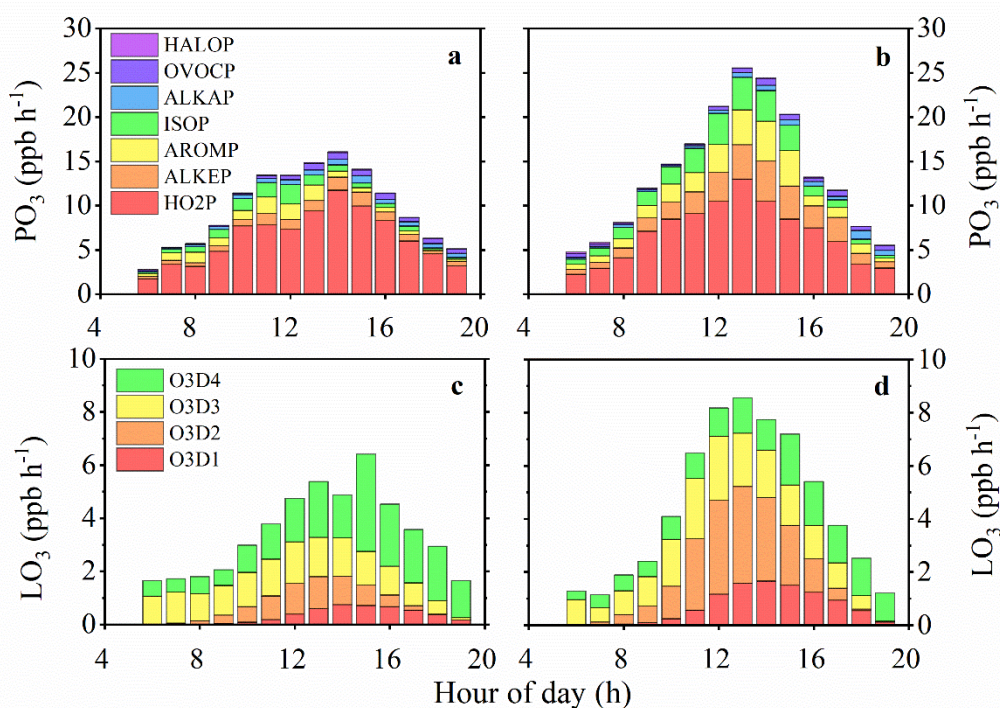
310 (ALKAP), alkene-derived (ALKEP), aromatic-derived (AROMP), isoprene-derived (ISOP),  
311 oxygenated-VOC-derived (OVOCP), and halohydrocarbon-derived (HALOP) RO<sub>2</sub> and HO<sub>2</sub>P.  
312 The ozone destruction processes included the reaction between O<sub>3</sub> and HO<sub>x</sub> (O3D1), the  
313 reaction between O1D and H<sub>2</sub>O (O3D2), the reaction between O<sub>3</sub> and alkenes (O3D3), and the  
314 reaction between NO<sub>2</sub> and OH (O3D4).

315       Based on the observed VOCs (or PIC-VOCs), a fast O<sub>3</sub> production rate was observed at  
316 14:00 (or 13:00), with a diurnal maximum value of 16.1 (or 25.6) ppb h<sup>-1</sup> (Figure 3a and 3b),  
317 while the peak destruction rate was 6.4 (or 8.6) ppb h<sup>-1</sup> at 15:00 (or 13:00) (Figure 3c and 3d).  
318 The average daytime P(O<sub>3</sub>) from 07:00 to 19:00 based on the initial concentrations of VOCs  
319 was 4.0±3.1 ppb h<sup>-1</sup> higher than that based on the measured VOCs concentrations (Figure 3b).  
320 At the same time, the F(O<sub>3</sub>) from 07:00 to 19:00 based on the initial concentrations of VOCs  
321 was also 3.0±2.1 ppb h<sup>-1</sup> higher than the measured counterpart (Figure S12). Thus, the net O<sub>3</sub>  
322 production could be accumulatively underestimated by ~36 ppb day<sup>-1</sup> from 07:00 to 19:00 if  
323 the consumption of VOCs was not considered. This meant that the contribution of the local  
324 formation of O<sub>3</sub> could be underestimated using the directly measured VOCs concentrations. It  
325 should be pointed out that it is better to compare O<sub>3</sub> production with the true metric for O<sub>3</sub>  
326 production. However, it is impossible to directly measure the true metric for O<sub>3</sub> production in  
327 the atmosphere at the present time to know how well the method presented here corrects for  
328 that underestimation. In addition, the ozone concentrations must be constrained when  
329 simulating the ozone formation process (Lu et al., 2013; Tan et al., 2017). Thus, it is impossible  
330 to directly compare the ozone production based on PIC-VOCs with that using measured VOCs

331 concentrations. Therefore, we alternatively compared the integrated net ozone production rates  
332 rather than ozone production or concentrations between the two scenarios. An upwind O<sub>3</sub> and  
333 VOCs measurement combined with a trajectory analysis might provide an approach for  
334 checking the accuracy of our results. Alternatively, conducting a transient O<sub>3</sub> production rate  
335 analysis after subtracting the transport of O<sub>3</sub> with a regional model and/or satellite observation  
336 might be another option. Unfortunately, neither the upwind measurement nor the regional  
337 model simulation was available at the time of our study. To further check the accuracy of our  
338 results, we chose August 4<sup>th</sup> as a test case to explore the influence of the transport of ozone on  
339 a downwind site based on the trajectory analysis. As shown in Figure S13, the mean ozone  
340 concentration of the downwind site (national monitoring station, NMS) was 27.6±21.9 ppb  
341 day<sup>-1</sup> higher than that of the observation site (OS), which was slightly less than the difference  
342 (~36 ppb day<sup>-1</sup>) between PIC-VOCs and observed VOCs and indirectly rationalized our results.

343 The HO<sub>2</sub> path contributed 64.8% to the total ozone formation on average, which was  
344 slightly higher than the reported value (57.0%) in Wangdu (Tan et al., 2018), whereas the RO<sub>2</sub>  
345 path, in which aromatics (9.4%), alkenes (8.4%), isoprene (7.8%), alkanes (4.7%), OVOCs  
346 (4.3%) and halohydrocarbons (0.6%) were the main contributors, contributed to the remaining  
347 part. For the PIC-VOCs, the dominant path of O<sub>3</sub> production (51.7%) was still the HO<sub>2</sub> path,  
348 followed by the RO<sub>2</sub> path related to alkenes (14.7%), aromatics (12.8%), and isoprene (11.7%).  
349 The relative contribution of the RO<sub>2</sub> path to P(O<sub>3</sub>) increased by 13.4% compared with the  
350 measured VOCs, particularly alkene-derived RO<sub>2</sub>, which increased by 10.2%. As shown in  
351 Figure 3c and 3d, the destruction of total oxidants was dominated by the reaction between O<sub>3</sub>

352 and alkenes (O3D3) in the morning. It gradually shifted to the reaction between NO<sub>2</sub> and OH  
353 (O3D4) from 11:00 to 16:00 and the photolysis of O<sub>3</sub> followed by a reaction with water (O3D2)  
354 from 12:00 to 15:00 because O<sub>3</sub> concentration increased while NO<sub>2</sub> decreased (Figure 3c).  
355 Figure S14 shows the percentages of the different paths of P(O<sub>3</sub>) and L(O<sub>3</sub>). The relative  
356 contributions of the reactions between O<sub>3</sub> and alkenes (O1D3) and between NO<sub>2</sub> and OH  
357 (O1D4) to the O<sub>3</sub> sinks decreased when calculated based on PIC-VOCs compared with those  
358 of the measured VOCs, while they obviously increased for the other two paths, i.e., O3D1 and  
359 O3O2. The O<sub>3</sub> destruction of the HO<sub>x</sub> and O<sub>3</sub> reaction (O3D1) gradually increased with the  
360 continuous photochemical reaction. In addition, the maximum O<sub>3</sub> formation rates of the RO<sub>2</sub>  
361 derived from OVOCs and halohydrocarbons were 0.75 and 0.18 ppb h<sup>-1</sup>, respectively. These  
362 values could be underestimated due to the incomplete gas reaction mechanism of OVOCs and  
363 halohydrocarbons in MCM3.3.1. In general, the measured VOCs as model inputs could fail to  
364 truly reflect the oxidation capacity and underestimate the local formation of O<sub>3</sub> and organic  
365 aerosols (Zhan et al., 2021).



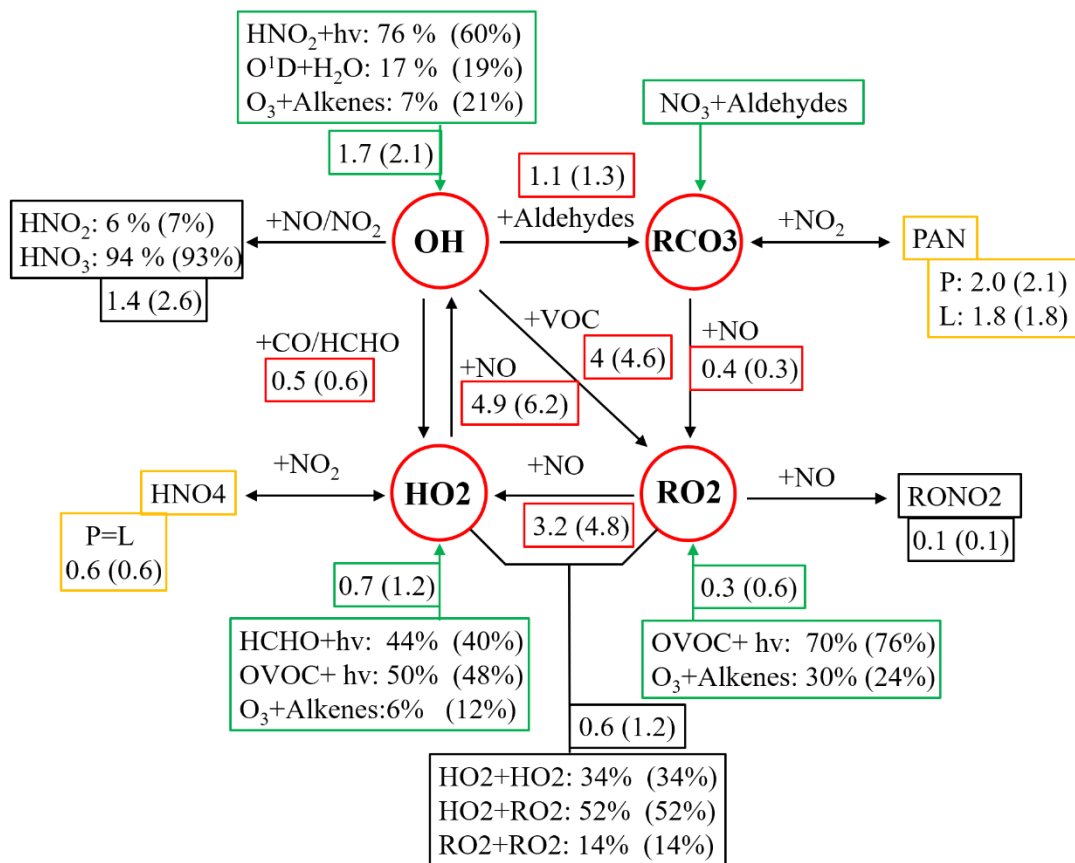
366

367 **Figure 3.** Mean diurnal profile of the instantaneous ozone production and destruction rate  
 368 calculated from the MCM-OBM model (instantaneous ozone rate derived from observed VOCs  
 369 in a and c and from PIC-VOCs in b and d). The upper panel presents the speciation of the ozone  
 370 formation rate. The lower panel presents the speciation of the ozone destruction rate. The data  
 371 range is August 1-28, 2019.

372

373 The budget of OH-HO<sub>2</sub>-RO<sub>2</sub> radicals was further analysed to understand the  
 374 photochemical O<sub>3</sub> formation process. The comparison of the radical budget derived from the  
 375 observed and PIC-VOCs is shown in Figure 4. The radical cycles are divided into radical  
 376 sources (green boxes), radical sinks (black boxes), radical propagations (red circles) and  
 377 equilibria between radical and reservoir species (yellow boxes). The numbers or percentages  
 378 are the average formation rates (ppb h<sup>-1</sup>) or relative contributions of the corresponding reaction  
 379 path based on the observed VOCs (outside the brackets) and the PIC-VOCs (inside the brackets)

380 to a certain radical. The relative contributions of different radical paths based on the observed  
381 VOCs (outside the brackets) were comparable with those reported in Beijing, Shanghai, and  
382 Guangzhou (Tan et al., 2019), while variations were observed for some reaction paths based  
383 on the PIC-VOCs. For example, the reaction between ozone and alkenes based on initial VOC  
384 concentrations (percentages inside the brackets) contributed more to OH (from 7% to 21%)  
385 and HO<sub>2</sub> radical production (from 6% to 12%), while photolysis of HONO and HCHO  
386 contributed less to the production of OH (from 76% to 60%) and HO<sub>2</sub> radicals (from 44% to  
387 40%), respectively. Other radical sources were consistent between the two scenarios.  
388 Interestingly, the average formation rates of OH, HO<sub>2</sub> and RO<sub>2</sub> radicals derived from the PIC-  
389 VOCs were obviously higher than those from the observed VOCs. In particular, the oxidation  
390 of NO by RO<sub>2</sub> and HO<sub>2</sub> increased by 1.6 and 1.3 ppb h<sup>-1</sup>, respectively. The enhanced oxidation  
391 rate of NO was equal to the increase in the average F(O<sub>3</sub>) in the analysis process above. This  
392 meant that the radical propagation of OH-RO<sub>2</sub>-HO<sub>2</sub> sped up in the case of PIC-VOCs,  
393 subsequently accelerating the chemical loop of NO-NO<sub>2</sub>-O<sub>3</sub>. For the radical sinks and equilibria  
394 related to HNO<sub>4</sub>, RONO<sub>2</sub> and PAN, the values were basically comparable between the two  
395 scenarios. In addition, the O<sub>3</sub> formation from the RO<sub>2</sub> path increased by 4.1% (from 39.5% to  
396 43.6%) in the simulation using the PIC-VOCs compared with the observed VOCs. The above  
397 budget analysis explained the observed increases in F(O<sub>3</sub>) (~3 ppb h<sup>-1</sup>), which were mainly  
398 driven by the reaction of missed reactive VOCs, such as alkenes, with O<sub>3</sub>.



399

400 **Figure 4.** Comparison of the OH-HO<sub>2</sub>-RO<sub>2</sub> radical budget derived from the observed and PIC-  
 401 VOCs under daytime conditions (07:00 to 19:00 LT). The green, black, red and yellow boxes  
 402 denote the sources of radicals, radical sinks, radical propagation, and racial equilibrium,  
 403 respectively. The numbers or percentages outside and inside the brackets are the average  
 404 formation rates (ppb h<sup>-1</sup>) or relative contributions to a specific radical of the corresponding  
 405 reaction path based on observed VOCs and PIC-VOCs, respectively.

### 406 3.4 In situ O<sub>3</sub> formation process

407 In addition to chemical processes, which can be simulated using the OBM-MCM model,  
 408 transport processes, including horizontal, vertical transportation and dry deposition processes  
 409 (Tan et al., 2019), also have an important influence on the O<sub>3</sub> concentration. Thus, the change  
 410 in instantaneous ozone concentration can reflect the combined effect between photochemical

411 and physical transport processes (Tan et al., 2019). This change can be expressed as,

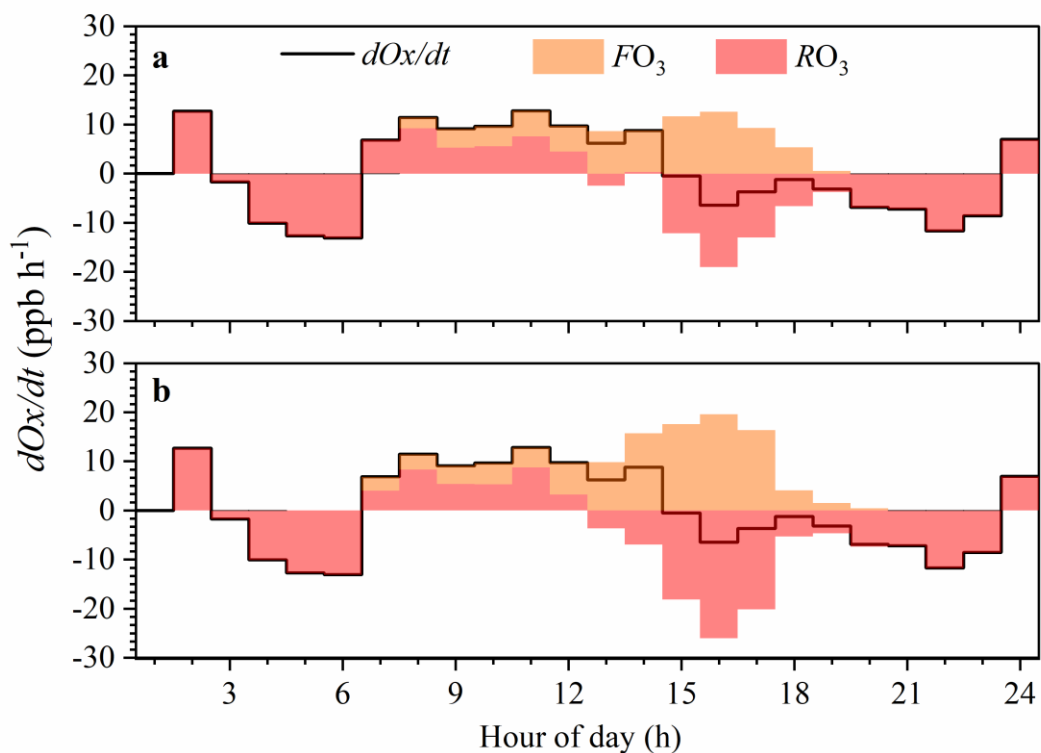
412 
$$\frac{dO_x}{dt} = F(O_3) + R(O_3) \quad (6)$$

413 where  $dO_x/dt$  is the  $O_3$  concentration change rate based on the measured data ( $\text{ppb h}^{-1}$ );  $F(O_3)$

414 is the net  $O_3$  formation rate ( $\text{ppb h}^{-1}$ ), and  $R(O_3)$  indicates transportation ( $\text{ppb h}^{-1}$ ). A positive

415 value of  $R(O_3)$  indicates an inflow of  $O_3$  with air mass and vice versa.  $O_3$  was replaced with Ox

416 ( $O_3 + NO_2$ ) to correct the titration of  $O_3$  by NO (Pan et al., 2015).



417 **Fig. 5.** The variation in Ox concentration and formation rate during an  $O_3$  pollution episode

418 (Aug. 1<sup>st</sup>). (a and b present the local ozone formation processes of the measured and PIC-VOCs,

419 respectively.)

420

421 The  $O_3$  budget analysis was performed during an  $O_3$  pollution episode (Aug. 1<sup>st</sup>). Figure

422 5 shows the simulated local ozone formation process based on the measured and PIC-VOCs.

423 The hourly variation in  $O_3$  concentrations from 19:00 to 6:00 the next day was dominated by  
424 regional transportation without  $O_3$  formation, while local photochemical  $O_3$  formation could  
425 explain all or part of the  $O_3$  concentration change during the time window from 07:00 to 19:00.  
426 The  $d(O_3)/dt$  shows an increase from 07:00 to 15:00 LT. However,  $d(O_3)/dt$  sharply changed to  
427 negative values at 16:00, which was consistent with diurnal  $O_3$  (the  $O_3$  peaks at 15:00) in Figure  
428 1.

429 The average daytime  $F(O_3)$  based on the observed and photochemical initial  
430 concentrations was  $6.4 \pm 4.0$  and  $8.9 \pm 6.7$  ppb  $h^{-1}$ , respectively. Photochemical  $O_3$  formation  
431 under both conditions started at 07:00 and reached maximum values of 12.6 and 19.6 ppb  $h^{-1}$   
432 at 15:00, respectively. The maximum daily value of  $P(O_3)$  was higher than those in the urban  
433 areas of Japan, America, and England (Whalley et al., 2018; Ren et al., 2006; Griffith et al.,  
434 2016; Kanaya et al., 2009) and lower than those in the suburbs of Guangzhou (Lu et al., 2012)  
435 and the urban areas and suburbs of Beijing (Lu et al., 2013). Before 12:00, the  $O_3$  formation  
436 rate based on the PIC-VOCs was slightly higher than that based on the measured VOCs, while  
437 both rates were within a range of 2.0~6.5 ppb  $h^{-1}$ . From 12:00 to 17:00, the  $O_3$  formation rate  
438 based on the PIC-VOCs and the observed concentration of VOCs greatly increased due to  
439 active photochemistry.

440 As shown in Figure 5, the increased  $O_3$  concentration was larger than the local  $O_3$   
441 photochemical production from 07:00 to 12:00 ( $R(O_3)$  was positive). This was mainly because,  
442 under stable conditions, the nighttime residual layer (RL) is isolated from mixing with the  
443 nighttime surface layer (Tan et al., 2021). The RL layer usually contains an air mass with a



444 higher ozone mixing ratio than in the surface layer. In the morning, surface heating causes  
445 mixing upward in the surface layer until the temperature inversion is eroded away and rapid  
446 mixing of pollutants throughout the surface and boundary layer occurs. However,  $R(O_3)$  was  
447 negative in the afternoon, which indicated that the local  $O_3$  formation at the measurement site  
448 contributed to not only the changes in the in situ  $O_3$  concentration but also the  $O_3$  source of the  
449 downwind regions. This was more clearly shown in Figure 4B under the PIC-VOCs condition.  
450 These results illustrated that local  $O_3$  photochemistry played a crucial role in both the local and  
451 regional  $O_3$  concentrations, which can be underestimated if consumed VOCs with high  
452 reactivities are ignored.

#### 453 **4. Conclusions**

454 In this study, we presented the local  $O_3$  formation process in August 2019 in Beijing based  
455 on the concentrations of observed and PIC-VOCs. The mean diurnal profile of  $O_3$  was  
456 unimodal with a peak at 15:00, while  $NO_x$  and observed TVOCs showed an opposite diurnal  
457 curve, and the PICs of TVOCs showed a different diurnal curve compared with that of the  
458 observed VOCs, with a slight increase from 07:00 to 14:00. The EKMA curve indicated that  
459 instantaneous  $O_3$  production was dependent on the real-time concentrations of  $NO_x$  and VOCs,  
460 i.e., the VOC-limited regime in the morning (09:00-10:00) and the  $NO_x$ -limited regime at noon  
461 (14:00-15:00). The sensitivity regime of  $O_3$  formation could be misdiagnosed if the consumed  
462 VOCs are not considered, for example, the VOC-limited regime (observed) shift to a transition  
463 regime (PIC-VOCs) in the morning is ignored. The mean  $F(O_3)$  based on PIC-VOCs was 3.0  
464  $ppb\ h^{-1}$  higher than that based on the measured VOCs, indicating that the underestimation of

465 local photochemistry in the local O<sub>3</sub> concentration could reach ~36 ppb day<sup>-1</sup> if the consumed  
466 VOCs are not accounted for. And the mean ozone concentration of downwind site was 27.6  
467 ppb day<sup>-1</sup> higher than the observation site, slightly lower than the difference (~36 ppb day<sup>-1</sup>)  
468 between PIC-VOCs and observed VOCs, which indirectly supported the accuracy of the above  
469 results. The radical budget analysis explained the observed increases in F(O<sub>3</sub>) (3 ppb h<sup>-1</sup>), which  
470 were mainly driven by the reaction of missed reactive VOCs, such as alkenes, with O<sub>3</sub>. In  
471 addition, the OH-HO<sub>2</sub> radical cycle was obviously accelerated by highly reactive alkenes after  
472 the photochemical loss of VOCs was accounted for. Finally, the results of the in situ O<sub>3</sub>  
473 formation process indicated that local O<sub>3</sub> photochemical formation played a key role in both  
474 local and regional O<sub>3</sub> concentrations. In conclusion, our results suggested that PIC-VOCs were  
475 more suitable than the observed VOC concentrations for diagnosing O<sub>3</sub> formation sensitivity.  
476

477 **Author contributions:** Wei Ma: Methodology, data curation, and writing of the original draft;  
478 Zemin Feng: Methodology, investigation, data curation, and writing of the original draft; Junlei  
479 Zhan: Methodology, investigation, data curation; Yongchun Liu: Conceptualization,  
480 investigation, data curation, writing, reviewing & editing, supervision, and funding acquisition;  
481 Pengfei Liu: Methodology, investigation, data curation, writing, reviewing & editing;  
482 Chengtang Liu: Methodology, investigation, data curation, writing, reviewing & editing;  
483 Qingxin Ma: Methodology, investigation, data curation; Kang Yang: Methodology,  
484 investigation, data curation. Yafei Wang: Methodology, investigation, resources, data curation;  
485 Hong He: Resources, writing, reviewing & editing; Markku Kulmala: Methodology, writing,  
486 reviewing & editing; Yujing Mu: Conceptualization, methodology, data curation, writing,  
487 reviewing & editing. Junfeng Liu: Conceptualization, methodology, data curation, writing,  
488 reviewing & editing, and supervision.

489 **Competing interests:** The authors declare that they have no substantive conflicts of interest.

490 **Data availability:** Data are available upon request to Yongchun Liu ([liuyc@buct.edu.cn](mailto:liuyc@buct.edu.cn)).

491 **Acknowledgements:** This research was financially supported by the National Natural Science  
492 Foundation of China (41877306, 92044301, 21976190), the Ministry of Science and  
493 Technology of the People's Republic of China (2019YFC0214701), the Strategic Priority  
494 Research Program of the Chinese Academy of Sciences and Beijing University of Chemical  
495 Technology.

496

497

## 498 Reference

- 499 Atkinson, R. and Arey, J.: Atmospheric degradation of volatile organic compounds, *Chemical Reviews*, 103, 4605-  
500 4638, <https://doi.org/10.1021/cr0206420>, 2003.
- 501 Carter, W. P. L.: Development of Ozone Reactivity Scales for Volatile Organic Compounds. 1994a, *J. Air Waste*  
502 *Manage. Assoc.*, 44, 881-899, <https://doi.org/10.1080/1073161X.1994.10467290>, 1994.
- 503 Chen, T., Liu, J., Liu, Y., and Ma, Q. G., Yanli; Zhong, Cheng; Jiang, Haotian; Chu, Biwu; Zhang, Peng; Ma, Jinzhu;  
504 Liu, Pengfei; Wang, Yafei; Mu, Yujing; He, Hong: Chemical characterization of submicron aerosol in summertime  
505 Beijing: A case study in southern suburbs in 2018, *Chemosphere*, 247, 125918,  
506 <https://doi.org/10.1016/j.chemosphere.2020.125918>, 2020.
- 507 Cohen, A. J., Brauer, M., Burnett, R., and Anderson, H. R. F., Joseph; Estep, Kara; Balakrishnan, Kalpana;  
508 Brunekreef, Bert; Dandona, Lalit; Dandona, Rakhi; Feigin, Valery; Freedman, Greg; Hubbell, Bryan; Jobling, Amelia;  
509 Kan, Haidong; Knibbs, Luke; Liu, Yang; Martin, Randall; Morawska, Lidia; Pope, C. Arden, III; Shin, Hwashin;  
510 Straif, Kurt; Shaddick, Gavin; Thomas, Matthew; van Dingenen, Rita; van Donkelaar, Aaron; Vos, Theo;  
511 Murray, Christopher J. L.; Forouzanfar, Mohammad H.: Estimates and 25-year trends of the global burden of disease  
512 attributable to ambient air pollution: an analysis of data from the Global Burden of Diseases Study 2015, *Lancet*,  
513 389, 1907-1918, [https://doi.org/10.1016/s0140-6736\(17\)30505-6](https://doi.org/10.1016/s0140-6736(17)30505-6), 2017.
- 514 Dang, R. and Liao, h.: Radiative Forcing and Health Impact of Aerosols and Ozone in China as the Consequence  
515 of Clean Air Actions over 2012–2017, *J Geophysical Research Letters*, 46, 12511-12519,  
516 <https://doi.org/10.1029/2019GL084605>, 2019.
- 517 Feng, Z., De Marco, A., Anav, A., Gualtieri, M., Sicard, P., Tian, H., Fornasier, F., Tao, F., Guo, A., and Paoletti,  
518 E.: Economic losses due to ozone impacts on human health, forest productivity and crop yield across China,  
519 *Environment International*, 131, 104966, <https://doi.org/10.1016/j.envint.2019.104966>, 2019.
- 520 Gao, J., Zhang, J., Li, H., Li, L., and Xu, L. Z., Yujie; Wang, Zhanshan; Wang, Xuezhong; Zhang, Weiqi;  
521 Chen, Yizhen; Cheng, Xi; Zhang, Hao; Peng, Liang; Chai, Fahe; Wei, Yongjie: Comparative study of volatile organic  
522 compounds in ambient air using observed mixing ratios and initial mixing ratios taking chemical loss into account  
523 - A case study in a typical urban area in Beijing, *Science of the Total Environment*, 628-629, 791-804,  
524 <https://doi.org/10.1016/j.scitotenv.2018.01.175>, 2018.
- 525 Gao, Y., Li, M., Wan, X., Zhao, X., Wu, Y., Liu, X., and Li, X.: Important contributions of alkenes and aromatics  
526 to VOCs emissions, chemistry and secondary pollutants formation at an industrial site of central eastern China,  
527 *Atmospheric Environment*, 244, 117927, <https://doi.org/10.1016/j.atmosenv.2020.117927>, 2021.
- 528 Goldan, P. D., Parrish, D. D., Kuster, W. C., Trainer, M., Mckeen, S. A., Holloway, J., Jobson, B. T., Sueper, D.  
529 T., and Fehsenfeld, F. C.: Airborne measurements of isoprene, CO, and anthropogenic hydrocarbons and their  
530 implications, *Journal of Geophysical Research-Atmospheres*, 105, 9091-9105,  
531 <http://doi.org/10.1029/1999JD900429>, 2000.
- 532 Griffith, S. M., Hansen, R. F., Dusanter, S., Michoud, V., Gilman, J. B., Kuster, W. C., Veres, P. R., Graus, M., de  
533 Gouw, J. A., Roberts, J., Young, C., Washenfelder, R., Brown, S. S., Thalman, R., Waxman, E., Volkamer, R., Tsai,  
534 C., Stutz, J., Flynn, J. H., Grossberg, N., Lefer, B., Alvarez, S. L., Rappenglueck, B., Mielke, L. H., Osthoff, H.  
535 D., and Stevens, P. S.: Measurements of hydroxyl and hydroperoxy radicals during CalNex-LA: Model  
536 comparisons and radical budgets, *Journal of Geophysical Research-Atmospheres*, 121, 4211-4232,  
537 <https://doi.org/10.1002/2015jd024358>, 2016.
- 538 Han, D., Wang, Z., Cheng, J., Wang, Q., Chen, X., and Wang, H.: Volatile organic compounds (VOCs) during

539 non-haze and haze days in Shanghai: characterization and secondary organic aerosol (SOA) formation,  
540 Environmental Science and Pollution Research, 24, 18619-18629, <https://doi.org/10.1007/s11356-017-9433-3>,  
541 2017.

542 He, Z., Wang, X., Ling, Z., Zhao, J., Guo, H., Shao, M., and Wang, Z.: Contributions of different anthropogenic  
543 volatile organic compound sources to ozone formation at a receptor site in the Pearl River Delta region and its  
544 policy implications, Atmospheric Chemistry and Physics, 19, 8801-8816, [https://doi.org/10.5194/acp-19-8801-](https://doi.org/10.5194/acp-19-8801-2019)  
545 [2019](https://doi.org/10.5194/acp-19-8801-2019), 2019.

546 Jobson, B. T., Berkowitz, C. M., Kuster, W. C., Goldan, P. D., Williams, E. J., Fesenfeld, F. C., Apel, E. C., Karl,  
547 T., Lonneman, W. A., and Riemer, D.: Hydrocarbon source signatures in Houston, Texas: Influence of the  
548 petrochemical industry, Journal of Geophysical Research-Atmospheres, 109,  
549 <http://doi.org/10.1029/2004jd004887>, 2004.

550 Kanaya, Y., Pochanart, P., Liu, Y. L., J.; Tanimoto, H., Kato, S., Suthawaree, J., Inomata, S., Taketani, F., Okuzawa,  
551 K., Kawamura, K., Akimoto, H., and Wang, Z. F.: Rates and regimes of photochemical ozone production over  
552 Central East China in June 2006: a box model analysis using comprehensive measurements of ozone precursors,  
553 Atmospheric Chemistry and Physics, 9, 7711-7723, <https://doi.org/10.5194/acp-9-7711-2009>, 2009.

554 Li, J., Wu, R., Li, Y., Hao, Y., and Xie, S. Z., Liming;: Effects of rigorous emission controls on reducing ambient  
555 volatile organic compounds in Beijing, China, Science of the Total Environment, 557, 531-541,  
556 <https://doi.org/10.1016/j.scitotenv.2016.03.140>, 2016a.

557 Li, J., Yang, W., Wang, Z., Chen, H., Hu, B., Li, J., Sun, Y., Fu, P., and Zhang, Y.: Modeling study of surface ozone  
558 source-receptor relationships in East Asia, Atmospheric Research, 167, 77-88,  
559 <https://doi.org/10.1016/j.atmosres.2015.07.010>, 2016b.

560 Li, L., An, J. Y., Shi, Y. Y., and Zhou, M. Y., R. S; Huang, C; Wang, H. L; Lou, S. R; Wang, Q; Lu, Q; Wu, J.:  
561 Source apportionment of surface ozone in the Yangtze River Delta, China in the summer of 2013, Atmospheric  
562 Environment, 144, 194-207, <https://doi.org/10.1016/j.atmosenv.2016.08.076>, 2016c.

563 Li, M., Zhang, Q., Zheng, B., Tong, D., Lei, Y., Liu, F., Hong, C., Kang, S., Yan, L., Zhang, Y., Bo, Y. S., Hang,  
564 Cheng, Y., and He, K.: Persistent growth of anthropogenic non-methane volatile organic compound (NMVOC)  
565 emissions in China during 1990-2017: drivers, speciation and ozone formation potential, Atmospheric Chemistry  
566 and Physics, 19, 8897-8913, <https://doi.org/10.5194/acp-19-8897-2019>, 2019.

567 Ling, Z. H. and Guo, H.: Contribution of VOC sources to photochemical ozone formation and its control policy  
568 implication in Hong Kong, Environmental Science & Policy, 38, 180-191,  
569 <https://doi.org/10.1016/j.envsci.2013.12.004>, 2014.

570 Liu, J., Li, X., Tan, Z., Wang, W., and Zhang, Y.: Assessing the Ratios of Formaldehyde and Glyoxal to NO<sub>2</sub> as  
571 Indicators of O<sub>3</sub>-NO<sub>x</sub>-VOC Sensitivity, Environmental Science Technology, 55, 10935-10945,  
572 <https://doi.org/10.1021/acs.est.0c07506>, 2021.

573 Liu, Y., Yan, C., Feng, Z., Zheng, F., and Kulmala, M.: Continuous and comprehensive atmospheric observations  
574 in Beijing: a station to understand the complex urban atmospheric environment, Big Earth Data, 4, 295-321,  
575 <https://doi.org/10.1080/20964471.2020.1798707>, 2020a.

576 Liu, Y., Ni, S., Jiang, T., Xing, S., Zhang, Y., Bao, X., Feng, Z., Fan, X., Zhang, L., and Feng, H.: Influence of  
577 Chinese New Year overlapping COVID-19 lockdown on HONO sources in Shijiazhuang, Science of the Total  
578 Environment, 745, 141025, <https://doi.org/10.1016/j.scitotenv.2020.141025>, 2020b.

579 Liu, Y., Zhang, Y., Lian, C., Yan, C., Feng, Z., Zheng, F., Fan, X., Chen, Y., Wang, W., Chu, B., Wang, Y., Cai, J.,  
580 Du, W., Daellenbach, K. R., Kangasluoma, J., Bianchi, F., Kujansuu, J., Petaja, T., Wang, X., Hu, B., Wang, Y.,

581 Ge, M., He, H., and Kulmala, M.: The promotion effect of nitrous acid on aerosol formation in wintertime in  
582 Beijing: the possible contribution of traffic-related emissions, *Atmospheric Chemistry and Physics*, 20, 13023-  
583 13040, <https://doi.org/10.5194/acp-20-13023-2020>, 2020c.

584 Lu, K. D., F. Rohrer; F. Holland, H. F., B. Bohn, T. Brauers, C. C. Chang, R. Haseler, M. Hu, K. Kita, and Y. K.,  
585 X. Li, S. R. Lou, S. Nehr, M. Shao, L. M. Zeng, A. Wahner, Y. H. Zhang, and A. Hofzumahaus: Observation and  
586 modelling of OH and HO<sub>2</sub> concentrations in the Pearl River Delta 2006: a missing OH source in a VOC rich  
587 atmosphere, *Atmospheric Chemistry and Physics*, 12, 1541-1569, <https://doi.org/10.5194/acp-12-1541-2012>,  
588 2012.

589 Lu, K. D., Hofzumahaus, A., Holland, F., Bohn, B., Brauers, T., Fuchs, H., Hu, M., Haeseler, R., Kita, K., Kondo,  
590 Y., Li, X., Lou, S. R., Oebel, A., Shao, M., Zeng, L. M., Wahner, A., Zhu, T., Zhang, Y. H., and Rohrer, F.: Missing  
591 OH source in a suburban environment near Beijing: observed and modelled OH and HO<sub>2</sub> concentrations in  
592 summer 2006, *Atmospheric Chemistry and Physics*, 13, 1057-1080, <https://doi.org/10.5194/acp-13-1057-2013>,  
593 2013.

594 Lu, X., Chen, N., Wang, Y., Cao, W., Zhu, B., Yao, T., Fung, J. C. H., and Lau, A. K. H.: Radical budget and ozone  
595 chemistry during autumn in the atmosphere of an urban site in central China, *Journal of Geophysical Research-  
596 Atmospheres*, 122, 3672-3685, <https://doi.org/10.1002/2016jd025676>, 2017.

597 Ma, J. K., Jyoti, Li, V. O. K., and Lam, J. C. K.: Effects of China's current Air Pollution Prevention and Control  
598 Action Plan on air pollution patterns, health risks and mortalities in Beijing 2014-2018, *Chemosphere*, 260,  
599 127572, <https://doi.org/10.1016/j.chemosphere.2020.127572>, 2020.

600 Ma, Z., Liu, C., Zhang, C., Liu, P., Ye, C., Xue, C., Zhao, D., Sun, J., Du, Y., Chai, F., and Mu, Y.: The levels,  
601 sources and reactivity of volatile organic compounds in a typical urban area of Northeast China, *Journal of  
602 Environmental Sciences*, 79, 121-134, <https://doi.org/10.1016/j.jes.2018.11.015>, 2019.

603 Mckeen, S. A., Liu, S. C., Hsie, E. Y., Lin, X., Bradshaw, J. D., Smyth, S., Gregory, G. L., and Blake, D. R.:  
604 Hydrocarbon ratios during PEM-WEST A: A model perspective, *Journal of Geophysical Research: Atmospheres*,  
605 101, 2087-2109, <https://doi.org/10.1029/95JD02733>, 1996.

606 Monks, P. S.: Gas-Phase Radical Chemistry in the Troposphere, *Chemical Society Reviews*, 34, 376-395,  
607 <https://doi.org/10.1039/B307982C>, 2005.

608 Pan, X., Kanaya, Y., Tanimoto, H., Inomata, S., Wang, Z., Kudo, S., and Uno, I.: Examining the major contributors  
609 of ozone pollution in a rural area of the Yangtze River Delta region during harvest season, *Atmospheric Chemistry  
610 and Physics*, 15, 6101-6111, <https://doi.org/10.5194/acp-15-6101-2015>, 2015.

611 Ren, X., Brune, W. H., Mao, J., Mitchell, M. J., Leshner, R. L., Simpas, J. B., Metcalf, A. R., Schwab, J. J., Cai, C.,  
612 Li, Y., Demerjian, K. L., Felton, H. D., Boynton, G., Adams, A., Perry, J., He, Y., Zhou, X., and Hou, J.: Behavior  
613 of OH and HO<sub>2</sub> in the winter atmosphere in New York city, *Atmospheric Environment*, 40, S252-S263,  
614 <https://doi.org/10.1016/j.atmosenv.2005.11.073>, 2006.

615 Seinfeld, J. H. and Pandis, S. N.: *Atmospheric chemistry and physics : from air pollution to climate change*  
616 (Second Edition), 2006.

617 Shao, M., Wang, B., Lu, S., Yuan, B., and Wang, M.: Effects of Beijing Olympics Control Measures on Reducing  
618 Reactive Hydrocarbon Species, *Environmental Science & Technology*, 45, 514-519,  
619 <https://doi.org/10.1021/es102357t>, 2011.

620 Tan, Z., Fuchs, H., Lu, K., and Hofzumahaus, A. B., Birger; Broch, Sebastian; Dong, Huabin; Gomm, Sebastian;  
621 Haeseler, Rolf; He, Lingyan; Holland, Frank; Li, Xin; Liu, Ying; Lu, Sihua; Rohrer, Franz; Shao, Min; Wang, Baolin;  
622 Wang, Ming; Wu, Yusheng; Zeng, Limin; Zhang, Yinsong; Wahner, Andreas; Zhang, Yuanhang: Radical chemistry

623 at a rural site (Wangdu) in the North China Plain: observation and model calculations of OH,HO<sub>2</sub> and RO<sub>2</sub> radicals,  
624 Atmospheric Chemistry and Physics, 17, 663-690, <https://doi.org/10.5194/acp-17-663-2017>, 2017.

625 Tan, Z., Lu, K., Jiang, M., Rong, S., and Zhang, Y.: Daytime atmospheric oxidation capacity in four Chinese  
626 megacities during the photochemically polluted season: A case study based on box model simulation, Atmospheric  
627 Chemistry Physics, 19, 3493-3513, <https://doi.org/10.5194/acp-19-3493-2019>, 2019.

628 Tan, Z., Lu, K., Jiang, M., Su, R., Dong, H., Zeng, L., Xie, S., Tan, Q., and Zhang, Y.: Exploring ozone pollution  
629 in Chengdu, southwestern China: A case study from radical chemistry to O<sub>3</sub>-VOC-NO<sub>x</sub> sensitivity, Science of the  
630 Total Environment, 636, 775-786, <https://doi.org/10.1016/j.scitotenv.2018.04.286>, 2018.

631 Tan, Z. F., Ma, X. F., Lu, K. D., Jiang, M. Q., Zou, Q., Wang, H. C., Zeng, L. M., and Zhang, Y. H.: Direct evidence  
632 of local photochemical production driven ozone episode in Beijing: A case study, Science of the Total Environment,  
633 800, <http://doi.org/10.1016/j.scitotenv.2021.148868>, 2021.

634 Wang, T., Xue, L., Brimblecombe, P., Lam, Y. F., Li, L., and Zhang, L.: Ozone pollution in China: A review of  
635 concentrations, meteorological influences, chemical precursors, and effects, Science of the Total Environment,  
636 575, 1582-1596, <https://doi.org/10.1016/j.scitotenv.2016.10.081>, 2017.

637 Whalley, L. K., Stone, D., Dunmore, R., Hamilton, J., Hopkins, J. R., Lee, J. D., Lewis, A. C., Williams, P.,  
638 Kleffmann, J., Laufs, S., Woodward-Massey, R., and Heard, D. E.: Understanding in situ ozone production in the  
639 summertime through radical observations and modelling studies during the Clean air for London project  
640 (ClearLo), Atmospheric Chemistry and Physics, 18, 2547-2571, <https://doi.org/10.5194/acp-18-2547-2018>, 2018.

641 Wiedinmyer, C., Friedfeld, S., Baugh, W., Greenberg, J., Guenther, A., Fraser, M., and Allen, D.: Measurement  
642 and analysis of atmospheric concentrations of isoprene and its reaction products in central Texas, Atmospheric  
643 Environment, 35, 1001-1013, [https://doi.org/10.1016/S1352-2310\(00\)00406-4](https://doi.org/10.1016/S1352-2310(00)00406-4), 2001.

644 Xie, Y., Dai, H., Zhang, Y., Wu, Y., Hanaoka, T., and Masui, T.: Comparison of health and economic impacts of  
645 PM<sub>2.5</sub> and ozone pollution in China, Environment International, 130, 104881,  
646 <https://doi.org/10.1016/j.envint.2019.05.075>, 2019.

647 Xue, L. K., Wang, T., Gao, J., Ding, A. J., Zhou, X. H., Blake, D. R., Wang, X. F., Saunders, S. M., Fan, S. J., Zuo,  
648 H. C., Zhang, Q. Z., and Wang, W. X.: Ground-level ozone in four Chinese cities: precursors, regional transport  
649 and heterogeneous processes, Atmospheric Chemistry and Physics, 14, 13175-13188, <https://doi.org/10.5194/acp-14-13175-2014>, 2014.

651 Yang, Y., Shao, M., Kessel, S., Li, Y. L., Keding, Lu, S. W., Jonathan, Zhang, Y., Zeng, L., Noelscher, A. C., Wu,  
652 Y., Wang, X., and Zheng, J.: How the OH reactivity affects the ozone production efficiency: case studies in Beijing  
653 and Heshan, China, Atmospheric Chemistry and Physics, 17, 7127-7142, <https://doi.org/10.5194/acp-17-7127-2017>, 2017.

655 Yuan, B., Hu, W. W., Shao, M., Wang, M., Chen, W. T., Lu, S. H., Zeng, L. M., and Hu, M.: VOC emissions,  
656 evolutions and contributions to SOA formation at a receptor site in eastern China, Atmospheric Chemistry and  
657 Physics, 13, 8815-8832, <https://doi.org/10.5194/acp-13-8815-2013>, 2013.

658 Zhan, J., Feng, Z., Liu, P., He, X., He, Z., Chen, T., Wang, Y., He, H., Mu, Y., and Liu, Y.: Ozone and SOA  
659 formation potential based on photochemical loss of VOCs during the Beijing summer, Environmental Pollution,  
660 285, 117444, <https://doi.org/10.1016/j.envpol.2021.117444>, 2021.

661 Zhang, K., Li, L., Huang, L., Wang, Y., Huo, J., Duan, Y., Wang, Y., and Fu, Q.: The impact of volatile organic  
662 compounds on ozone formation in the suburban area of Shanghai, Atmospheric Environment, 232, 117511,  
663 <https://doi.org/10.1016/j.atmosenv.2020.117511>, 2020.

664 Zhang, K., Huang, L., Li, Q., Huo, J., Duan, Y., Wang, Y., Yaluk, E., Wang, Y., Fu, Q., and Li, L.: Explicit modeling

665 of isoprene chemical processing in polluted air masses in suburban areas of the Yangtze River Delta region: radical  
666 cycling and formation of ozone and formaldehyde, *Atmospheric Chemistry and Physics*, 21, 5905-5917,  
667 <https://doi.org/10.5194/acp-21-5905-2021>, 2021a.

668 Zhang, M., Gao, W., Yan, J., Wu, Y., Marandino, C. A., Park, K., Chen, L., Lin, Q., Tan, G., and Pan, M.: An  
669 integrated sampler for shipboard underway measurement of dimethyl sulfide in surface seawater and air,  
670 *Atmospheric Environment*, 209, 86-91, <https://doi.org/10.1016/j.atmosenv.2019.04.022>, 2019.

671 Zhang, Q., Li, L., Zhao, W., Wang, X., Jiang, L., Liu, B., Li, X., and Lu, H.: Emission characteristics of VOCs  
672 from forests and its impact on regional air quality in Beijing, China *Environmental Science*, 41, 622-632,  
673 <https://doi.org/10.19674/j.cnki.issn1000-6923.2021.0072>, 2021b.

674 Zong, R. H., Xue, L. K., Wang, T. B., and Wang, W. X.: Inter-comparison of the Regional Atmospheric Chemistry  
675 Mechanism (RACM2) and Master Chemical Mechanism (MCM) on the simulation of acetaldehyde, *Atmospheric  
676 Environment*, 186, 144-149, <http://doi.org/10.1016/j.atmosenv.2018.05.013>, 2018.

677